

A Cryo-Electron Microscopy Study Identifies the Complete H16.V5 Epitope and Reveals Global Conformational Changes Initiated by Binding of the Neutralizing Antibody Fragment

Hyunwook Lee,^a Sarah A. Brendle,^b Stephanie M. Bywaters,^b Jian Guan,^a Robert E. Ashley,^a Joshua D. Yoder,^c Alexander M. Makhov,^c James F. Conway,^c Neil D. Christensen,^b Susan Hafenstein^a

Department of Medicine, The Pennsylvania State University College of Medicine, Hershey, Pennsylvania, USA^a; Department of Pathology, The Pennsylvania State University College of Medicine, Hershey, Pennsylvania, USA^b; Department of Structural Biology, University of Pittsburgh School of Medicine, Pittsburgh, Pennsylvania, USA^c

ABSTRACT

Human papillomavirus 16 (HPV16) is a worldwide health threat and an etiologic agent of cervical cancer. To understand the antigenic properties of HPV16, we pursued a structural study to elucidate HPV capsids and antibody interactions. The cryo-electron microscopy (cryo-EM) structures of a mature HPV16 particle and an altered capsid particle were solved individually and as complexes with fragment of antibody (Fab) from the neutralizing antibody H16.V5. Fitted crystal structures provided a pseudo-atomic model of the virus-Fab complex, which identified a precise footprint of H16.V5, including previously unrecognized residues. The altered-capsid-Fab complex map showed that binding of the Fab induced significant conformational changes that were not seen in the altered-capsid structure alone. These changes included more ordered surface loops, consolidated so-called “invading-arm” structures, and tighter intercapsomeric connections at the capsid floor. The H16.V5 Fab preferentially bound hexavalent capsomers likely with a stabilizing effect that directly correlated with the number of bound Fabs. Additional cryo-EM reconstructions of the virus-Fab complex for different incubation times and structural analysis provide a model for a hyperstabilization of the capsomer by H16.V5 Fab and showed that the Fab distinguishes subtle differences between antigenic sites.

IMPORTANCE

Our analysis of the cryo-EM reconstructions of the HPV16 capsids and virus-Fab complexes has identified the entire HPV.V5 conformational epitope and demonstrated a detailed neutralization mechanism of this clinically important monoclonal antibody against HPV16. The Fab bound and ordered the apical loops of HPV16. This conformational change was transmitted to the lower region of the capsomer, resulting in enhanced intercapsomeric interactions evidenced by the more ordered capsid floor and “invading-arm” structures. This study advances the understanding of the neutralization mechanism used by H16.V5.

Human papillomavirus (HPV) is a nonenveloped double-stranded DNA virus that can induce several epithelial cancers, especially cervical cancer (1–3). HPV16 is the most prevalent high-risk type of HPV (4, 5) and has been a primary target for the development of prophylactic vaccines (6, 7). HPV is epitheliotropic, and its replication is tightly associated with terminal differentiation of keratinocytes. This restricted tropism makes the production of high-titer preparations of authentic virion challenging. Alternative production methods have been developed to produce high-titer stocks of virus-like particles (VLP) (8), pseudovirions (PsV) (9), and quasivirions (QV) (10) while preserving the main attributes of the native capsid structure. These particles have been used successfully for vaccine development and for studies of antigenicity, receptor usage, entry mechanisms, and capsid structure.

The infectious HPV has a T=7 icosahedral capsid (55 to 60 nm in diameter), composed of 72 L1 capsid protein pentamers and up to 72 copies of L2 capsid protein located beneath the axial lumen of each L1 capsomer (11). Atomic structures of HPV16 L1-pentamers and a T=1 capsid have been solved by X-ray crystallography (12–14); however, the HPV T=7 capsid has been visualized only by cryo-electron microscopy (cryo-EM) reconstructions (11, 15–18). Twelve of the pentamers lie on the icosahedral 5-fold axes (pentavalent capsomers), whereas the other 60 pentamers are positioned at the pseudo 6-fold axes (hexavalent capsomers). The apical surface of each pentameric capsomer is comprised of anti-

genic loops (BC, DE, EF, FG, and HI loops from each L1 protein) that connect the eight antiparallel beta strands (BIDG and CHEF) that form the common jellyroll structural motif. These loops contain the highest sequence variations among the different HPV types and form the major neutralizing epitopes (19–23). The capsid floor is connected by N-terminal and C-terminal residues of L1 proteins, and these N- and C-terminal “arms” connect the pentameric capsomers into a T=7 icosahedral lattice (24). The HPV C-terminal “invading arm” extends to a neighboring pentamer and forms critical contacts between two subunits before looping back to rejoin the original donor capsomer. This “suspended-

Received 7 October 2014 Accepted 10 November 2014

Accepted manuscript posted online 12 November 2014

Citation Lee H, Brendle SA, Bywaters SM, Guan J, Ashley RE, Yoder JD, Makhov AM, Conway JF, Christensen ND, Hafenstein S. 2015. A cryo-electron microscopy study identifies the complete H16.V5 epitope and reveals global conformational changes initiated by binding of the neutralizing antibody fragment. *J Virol* 89:1428–1438. doi:10.1128/JVI.02898-14.

Editor: M. J. Imperiale

Address correspondence to Susan Hafenstein, shafenstein@hmc.psu.edu.

Copyright © 2015, American Society for Microbiology. All Rights Reserved.

doi:10.1128/JVI.02898-14

bridge” structure, separated from and raised above the capsid floor, was recently visualized in HPV16 (18).

There is a distinct maturation of HPV16 capsids that progresses as the correct intercapsomeric disulfide bonds are formed between cysteine residues in the C-terminal arms (C428) and surface loops (C175) (24–27). This disulfide bond formation regulates the stability of the HPV capsid and determines the assembly state of the virus (18, 25, 28). The known immature and mature HPV16 VLP 3D reconstructions show significant differences between the two capsid forms (18, 25). The immature capsid reconstruction identifies a lack of density in the capsid floor between the capsomers, whereas the mature form has a relatively closed capsid floor (18). The capsomers themselves are puffy and dome-shaped in the immature virus, but the mature virus has a tightly knit arrangement of L1 loops that form a star-shaped pattern with a depression at the center of each knob-like capsomer (18, 25). The mature capsid better correlates with the known atomic structures: HPV16 T=1 capsid (PDB accession code 1DZL) (13), pentameric L1 proteins (PDB accession codes 2R5H and 3OAE) (12, 14), and T=7 bovine papillomavirus (BPV) capsid (PDB accession code 3IYJ) (24). Thus, the complete intercapsomeric disulfide bonds, tighter capsomeric connection, and organized surface loops indicate a more mature stable capsid structure. However, the stabilization of capsid features and their relation to capsid antigenicity have not been studied.

H16.V5 is a HPV16 type-specific neutralizing antibody (29, 30) that is clinically important, as it represents the majority of neutralizing antibodies in HPV vaccine recipients (31) and is often used for the assessment of the integrity and antigenicity of VLP vaccine products (32). The antibody is known to recognize two loops of the L1 protein, the FG loop (residues 266 to 297) and the HI loop (339 to 365) (12, 30). H16.V5 neutralizes a viral infection by interfering with internalization of bound particles (33). Here, we present cryo-electron microscopy (cryo-EM) three-dimensional (3D) reconstructions of the mature and altered HPV16 virions and each of these two capsid types complexed with H16.V5 Fab fragments. The pseudoatomic model for the virus-Fab complex identifies the precise conformational epitope of the H16.V5 antibody that includes previously unknown additional components of the L1 epitopes targeted by H16.V5 that map to the BC and DE loops. Our work demonstrates the Fab-induced hyperstabilization of the capsid, which contributes to the neutralization mechanism of H16.V5.

MATERIALS AND METHODS

Virus preparation and purification. Briefly, the HPV16 quasivirus (QV16) used throughout for the structural studies was prepared by transfecting 293TT cells concurrently with the cottontail rabbit papillomavirus (CRPV) genome and an HPV16 L1/L2 expression vector as previously described (9, 26, 34, 35). Two days posttransfection, cells were harvested and lysed with Brij 58 detergent (Sigma-Aldrich). Lysates were incubated at 37°C for 24 h to allow QV16 to mature and then treated with the nuclease Benzonase (Sigma-Aldrich) and plasmid-safe ATP-dependent DNase (Epicentre) to ensure the removal of unencapsidated DNA. QV16 particles were purified by CsCl step gradient ultracentrifugation for 2 h at 25,000 rpm. The lower band was extracted and further purified using a linear CsCl gradient. Purified QV16 was dialyzed against NaCl using a centrifugal filter unit with a 30,000 molecular weight (MW) cutoff (Millipore) and subsequently dialyzed into phosphate-buffered saline (PBS). The lysate-buffering approach of Cardone et al. was not used in the current study (18).

Fab/antibody preparation. Monoclonal antibody (MAb) was produced as described previously (29, 34, 36, 37) and purified from hybridoma supernatants using the protein A IgG purification kit (Pierce). H16.V5 Fab was generated from the purified MAb using a Fab preparation kit (Pierce). Briefly, ~2 mg of purified MAb was prepared for digestion by passing the sample over a Zeba desalting spin column (Pierce). The H16.V5 MAb was then incubated in the presence of cysteine and papain at 37°C with end-over-end mixing for 3 h. Following incubation, the sample was purified using a protein A column, and Fabs were eluted with PBS.

Sequence determination of H16.V5 variable domain. The hybridoma cells were pelleted by centrifugation, and RNA was extracted using TRIzol reagent (Life Technologies). Total RNA was treated with DNase I (RNase-free) (New England BioLabs) to digest potential contaminating DNA in the sample. H16.V5 cDNAs were synthesized from treated RNA with the RevertAid first-strand cDNA synthesis kit (Thermo Scientific). The cDNAs were used as a template for PCR and amplified using PFU Turbo DNA polymerase (Agilent). PCR amplification utilized amplification primers previously described by Wang et al. (38). Immunoglobulin heavy chains were amplified using the IgG2b isotype-specific constant-region 3' primer and two highly degenerate 5' primers. The light chains were amplified using the 3' degenerate kappa chain constant-region primer and the 5' kappa chain framework one-region universal degenerate primer. Prior to sequencing, PCR products were purified using the QIAquick PCR purification kit (Qiagen). The primers used for PCR amplification were also used as sequencing primers to obtain initial sequences. Resolution of the 5' and 3' ends of the sequence required sequence-specific primers.

Cryo-EM imaging of the HPV16 capsids and virus-Fab complexes. Purified virus was concentrated (>5 mg/ml) and sonicated prior to vitrification (see Fig. 3A). The highly concentrated virus and H16.V5 Fab fragments were incubated for 5 min on ice with a molar ratio of 1:720 (capsid to Fab), providing an excess of 2 Fabs per each of the predicted 360 binding sites. For both HPV16 alone and HPV16-Fab complex, 3 µl of the sample were pipetted onto a Quantifoil grid (Quantifoil Micro Tools GmbH, Jena, Germany), blotted to remove excess sample, and plunge-frozen into a liquid ethane-propane mixture (39) using an Mk III Vitrobot (FEI, Hillsboro, OR). Low-dose conditions were used to record images on Kodak SO-163 film (Kodak, Rochester, NY) in an FEI TF-20 electron microscope operating at 200 kV with a nominal magnification of 50,000×. The microscope was equipped with a Gatan 626 cryoholder (Gatan, Inc., Pleasanton, CA). Cryo-EM images were collected with a defocus range of 2 to 4 µm for the capsid and 1 to 3 µm for the virus-Fab complex (Table 1). Films were scanned using a Nikon Super Coolscan 9000 (Nikon, Melville, NY), giving a nominal pixel size of 1.3 Å/pixel. A similar protocol was followed for the mature virus with and without Fab, except the sample concentration was limited to <1 mg/ml prior to vitrification. The samples were vitrified on Quantifoil holey carbon support grids (Quantifoil, Jena, Germany) that were plunged into liquid ethane using a Cryoplunge 3 (Gatan, Pleasanton, CA). Low-dose conditions were used to record digital images on an Ultrascan 4000 charge-coupled device (CCD) camera (Gatan, Pleasanton, CA) in a JEOL 2100 LaB₆ cryo-electron microscope (JEOL, Peabody, MA) operating at 200 kV and equipped with a Gatan 626 cryoholder. The recorded CCD data had calibrated pixel sizes of 1.48 Å/pixel and 2.86 Å/pixel at nominal magnifications of 80,000× and 40,000×, respectively, and were imaged within a defocus range of 0.6 to 5.6 µm (Table 1).

Single-particle reconstruction. The program suites AUTO3DEM (40) and EMAN2 (41) were used for image processing and 3D reconstructions of the HPV16 and HPV16-Fab complexes (Table 1). Semiautomatic particle selection was performed using EMAN2's e2boxer.py to obtain the particle coordinates, followed by particle extraction, linearization, normalization, and apodization of the images using Robem (40). Defocus and astigmatism values to perform contrast transfer function (CTF) correction were assessed using Robem for the extracted particles (Table 1). The icosahedrally averaged reconstructions were initiated using random mod-

TABLE 1 Image data for cryo-EM reconstructions

Particle type and sample prepn	Incubation time	No. of micrographs	Pixel size (Å/pixel)	Defocus level range (μm)	Total no. of particles	Particle no. used in maps	Final resolution (Å)	EMDB accession code
Altered								
Capsid	5 min	32	1.3	2.17–3.97	14,509	10,156	10.2	EMD-5991
Complex		35	1.3	1.80–3.36	3,222	2,898	10.4	EMD-5992
Mature								
Capsid	5 min	170	1.48	0.57–3.75	4,834	4,737	12.6	EMD-5993
Complex		411	1.48	0.69–3.99	2,306	2,075	13.6	EMD-5994
		1 h	138	2.86	1,155	1,040	14.7	EMD-6118
		72 h	102	2.86	1,326	1,127	15.8	EMD-6119

els generated from the raw data (42) (39) and reached 10- to 14-Å resolutions estimated where the Fourier shell correlation (FSC) dropped below 0.5 (Table 1). After refinement, the maps were sharpened with an inverse temperature factor of 1/(200 Å²).

Analysis of the capsid reconstructions for heterogeneous size. As done previously, a size-based classification scheme was used to characterize our data used in the HPV reconstructions (18). Two alternative mature-particle maps, 4% reduced and 4% expanded, were calculated by applying a magnification factor to the mature-particle reconstruction (40). Based on the PFT score that best correlated each projection with one of the three models, the data were classified into three subsets (18). The subsets were subsequently refined using the corresponding sized model (40). The same procedure was used to characterize homogeneity of the sample used to reconstruct the altered-capsid map.

Experimental reconstruction of altered capsid particles with the mature-virus search map. The 13-Å resolution map of the mature virus was calculated and scaled to match the pixel size of the altered-capsid images. With previously determined orientations and centers for the altered capsid particles, the input model was used for a local refinement of image origins and orientations using Parallel Orientation Refinement (POR) (40). A small subset of 10% of the particle projections that had the highest correlations with the input model was selected to produce the 3D map. Five iterations were performed, all output reconstructions were visually assessed, and the correlation coefficients between maps were calculated in UCSF Chimera (43).

Fitting of the capsomer and Fab structures. To obtain a 3D atomic model of the H16.V5 Fab, the amino acid sequence corresponding to the variable domain was submitted to Web Antibody Modeling (WAM) (44). This WAM model of the Fab variable domain and the crystal structure of the HPV16 pentamer (PDB accession code 3OAE) (14) were simultaneously fitted into the corresponding cryo-EM densities using Chimera (43). Due to steric interference, four of six Fabs were used within the virus icosahedral asymmetric unit in the fitting experiment. The fitting of the four Fabs and one pentamer was simultaneously refined by using Situs (45), giving a final correlation coefficient of 0.9233. A murine antibody crystal structure (PDB accession code 3GK8) was used for the constant domain of the Fab and was aligned to the fitted H16.V5 variable domain in Chimera (43). Contacts between the fitted crystal and WAM structures were identified using Chimera with the criteria for van der Waals overlap distances of −0.4 and 0.0 Å, respectively. The Fab binding surface area was calculated using a 1.4-Å probe through the CCP4 program AREAIMOL (46).

Radial projection, segmentation, and high-pass filtering of the reconstruction for figures. The spherical projections were generated in Robem (40) and Rivem (47). For the image in Fig. 4, the central section of the 3D map of the altered-capsid–Fab complex was CTF corrected by applying a Wiener filter. Difference maps were calculated from scaled cryo-EM maps of similar quality by subtracting the capsid density from the virus–Fab complex map using Robem (40). The difference maps were segmented (48), and the mean intensities of the segmented variable do-

main of the six Fabs on the asymmetric unit were measured in Chimera (43). To highlight the invading-arm structures, the Wiener-filtered 3D reconstruction of the virus–Fab complex was high-pass filtered with a cutoff spatial frequency of 16Å by EMAN2’s e2proc3d.py. The frequency was selected to visualize optimally the invading-arm structure. Visualization of the 3D structure was done in Chimera (43).

Map and structure accession numbers. Cryo-EM maps for the altered capsid, the capsid–Fab complex, the mature virus, the virus–Fab complex, the 1-h-incubation complex, and the 72-h-incubation complex have been deposited in the EM data bank (www.emdatabank.org/) under accession numbers EMD-5991, -5992, -5993, -5994, -6118, and -6119. Fitted structures of PDB accession codes 3OAE and the WAM have been deposited in the PDB under accession codes 3J7G and 3J7E, respectively.

RESULTS

The mature HPV16 capsid structure was obtained from purified capsids that were homogeneous. Similarly to what was done previously with HPV 16 VLP capsids (18), we performed a size-dependent classification experiment to determine if the quasivirus capsid particles were homogeneous. Of the purified quasivirus particles, 96.1% had capsids that were homogeneous in size, 600 Å in diameter. Only about 0.2% of the HPV16 quasivirus particles corresponded to a map that was 4% larger in diameter (data not shown), indicating that the HPV16 quasivirus sample did not contain a heterogeneous mixture of immature particles (18). The HPV16 mature-virus capsid map obtained a 13-Å resolution (Table 1) and displayed a T=7d icosahedral capsid structure (49). The capsomers had star-shaped morphology (Fig. 1A), consistent with a previously reported mature HPV16 VLP structure (18).

The complex map showed Fab density at each binding sites. The 14-Å virus–Fab complex map revealed density corresponding to a bound H16.V5 molecule at each of the 360 potential Fab binding sites on the capsid. Thus, five Fabs were bound on each capsomer, including the pentavalent capsomers on the icosahedral 5-fold symmetry axes (Fig. 1B). However, the Fab densities at the 5-fold were weaker, indicating a clash with the neighboring Fab bound to the hexavalent capsomer. This occupancy of Fab was inconsistent with a previous study that showed exclusive binding to the hexavalent capsomers (17). This discrepancy could be due to the different capsid forms used (L1-only VLP versus QV), different contour levels displayed for the maps, or other variations in experimental conditions, such as temperature and incubation time.

Fitting of the H16.V5 atomic model identified the complete conformational epitope. The H16.V5 atomic model based on the amino acid sequence (see Materials and Methods) (44) was fitted into the cryo-EM map of the mature-virus–Fab complex along

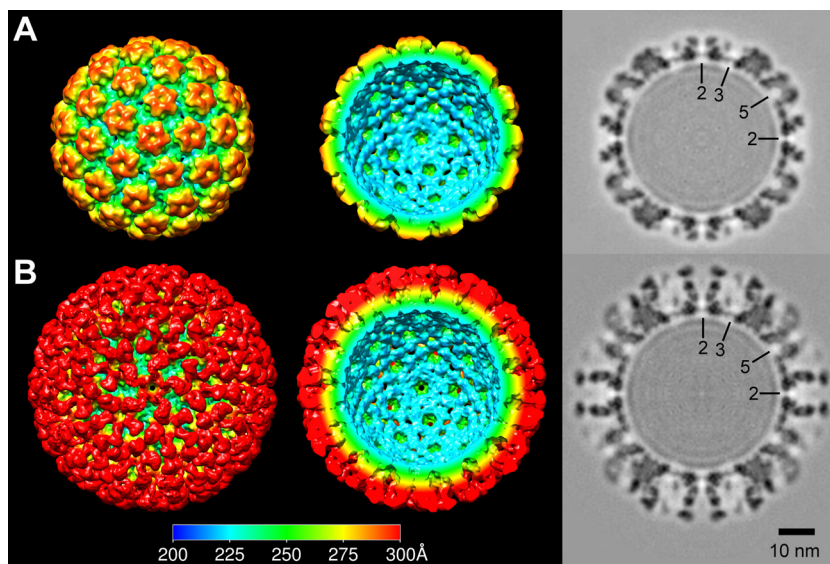


FIG 1 Cryo-EM 3D reconstructions of HPV16 and virus-H16.V5 Fab complex. (A) The 3D reconstruction of mature virus had a 600-Å diameter. (B) The virus-Fab complex map shows the mature virus decorated by H16.V5 Fab molecules and reveals that the Fabs bound the pentavalent capsomers on the 5-fold vertex. Surface-rendered images are oriented on an icosahedral 5-fold symmetry axis, and internal DNA was computationally removed (middle) to visualize the protein capsid shell. The rendered surfaces were radially colored according to the key and are displayed at a contour level of 1.0 σ above background. Central sections in standard orientation (on the 2-fold axis, with symmetry axes indicated in black) show the quality of the density (right).

with the X-ray crystal structure of the HPV16 pentamer (PDB accession code [3OAE](#)) (14) (Fig. 2A). Among the six Fabs bound to the virus within one icosahedral asymmetric unit, two Fab molecules sterically collided with each other. Because of the incom-

pleteness of the Fab densities due to the steric hindrance, only four of the Fabs (Fab-3 to -6) (Fig. 2A) on the hexavalent capsomers were fitted and refined. The fit was then replicated into the positions for the remaining two Fab molecules, Fab-1 and -2 (Fig. 2A).

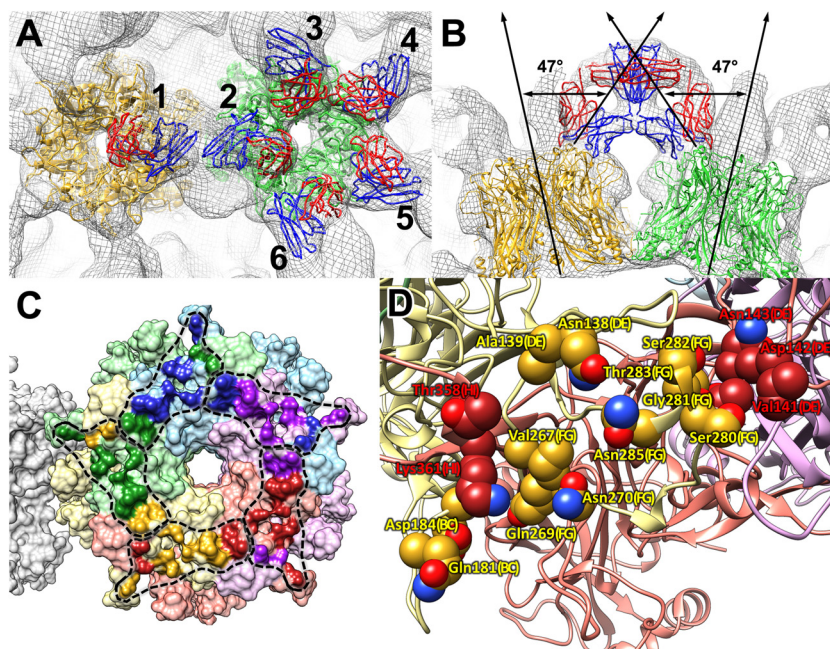


FIG 2 The pseudoatomic model was used to identify the Fab footprint. (A) The crystal structure of HPV16 pentamer (hexavalent and pentavalent capsomers are in green and yellow, respectively) and the atomic model of H16.V5 variable-domain (blue, heavy chain; red, light chain) were fitted into the density map. Fab-1 and -2 were replicated from the fitted Fab-3. The mature-virus-Fab cryo-EM density map is shown in gray mesh. (B) The side view of the Fab-1 and -2 bound on the pentavalent and hexavalent capsomers showed the steric clash between the two Fabs. The bound H16.V5 forms an angle of 47° relative to an axis through the center of the capsomer. (C) Each Fab binds across two L1 capsid proteins that are adjacent to one another. The contacting residues on the capsomeric surface are highlighted. Each L1 protein of the hexavalent capsomer is colored differently, and the pentavalent capsomer is in gray. The boundary of each Fab-binding residue is marked by a black dashed line. (D) The H16.V5 Fab bound 17 residues across five loops from two neighboring L1 proteins. The contacting residues are shown as spheres with the residue names and loops labeled.

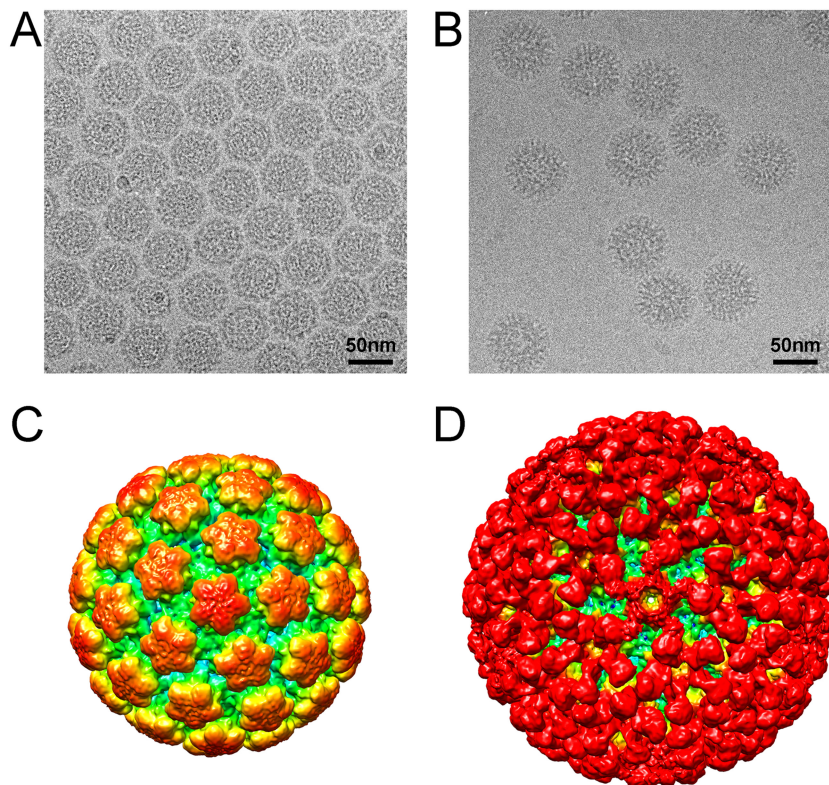


FIG 3 Cryo-EM images of the altered capsids and the capsid-Fab complexes with their corresponding 3D maps. Representative areas of the cryomicrographs illustrate homogeneous, intact capsids that were used for image reconstructions (A and C) and altered capsids incubated with excess H16.V5 Fab molecules (B and D). The altered capsids showed the characteristic puffy, inflated capsomers of an immature VLP (18). H16.V5 Fabs occupied all 360 binding sites of the capsid, but the Fab densities on the pentavalent capsomers were weaker than the densities on hexavalent capsomers. The rendered surfaces were radially colored according to the key and displayed at a contour level of 1.0σ above background.

The Fab bound to the capsomer surface with an angle of 47° through the pseudo dyad axis (Fig. 2B), and the heavy chain faced away from the center of the capsomer (Fig. 2B). When the constant domain of a murine antibody Fab (50) was fitted for Fab-1 and -2, the steric collision between the two Fabs was confirmed (Fig. 2B).

The Fab buried surface area was about $1,035 \text{ \AA}^2$, and the contacts within the Fab footprint mapped to the rim of the capsomer (Fig. 2C). Surprisingly, interactions were identified between the Fab and the DE and EF loops as well as with the FG and HI loops (Fig. 2D). The H16.V5 Fab bound where the antigenic loops from two L1 proteins are intertwined. Within the footprint, the first L1 protein (designated Left) contributes three loops, BC, FG, and DE, whereas the second L1 protein (designated Right) contributes HI and DE loops. Thus, there are five loops presented by two L1 proteins consecutively across the footprint, forming an intricate conformational epitope in a left-right-left-left-right L1 configuration (Fig. 2D). The footprint of H16.V5 suggests that the antibody interaction may hold the two L1 proteins together tightly, conferring a stabilizing force to the capsid.

The 3D reconstruction of a highly concentrated preparation of HPV16 showed different capsomeric structures. In a separate experiment with HPV16 and the subsequent structural determination, the purified quasivirus sample was highly concentrated (above 5 mg/ml) (Fig. 3A). This virus sample was incubated with H16.V5 Fab (Fig. 3B), and both the capsid and the virus-Fab com-

plex resulted in 10-Å-resolution maps (Fig. 3C and D; Table 1). The concentrated virus sample was intact, and no noticeable empty capsids resulting from DNA ejection were observed (Fig. 3A). A successful 10-Å reconstruction also confirmed that the concentrated particles were not damaged. Whereas the previous reconstruction was consistent with the mature HPV16 VLP structure (Fig. 1A), the reconstruction of overconcentrated particles (referred to here as altered particles or altered capsids) had features that resembled an immature VLP structure (25). Specifically, the apical surfaces of the capsomers were irregular and the center of each capsomer was inflated (Fig. 3C and 7A). Also, the densities corresponding to the intercapsomeric connections were attenuated compared to the mature virus. Unlike immature VLP, the altered HPV16 quasivirus had a radius similar to that of the mature particle (data not shown).

Even though the altered particles presented a seemingly homogeneous population (Fig. 3A), it was possible that the map resulted from averaging together particles from a heterogeneous population. Such a hybrid population might consist of a mixture of intact (mature) and compromised particle forms. To test this possibility, we used two approaches. First, we applied the size-based classification that was used for the mature particles (see Materials and Methods). The particles were homogeneous with only 1.3% of the particles, correlating better with a 4% larger map (data not shown).

In a second approach, a map of the mature virus (Fig. 1A) was

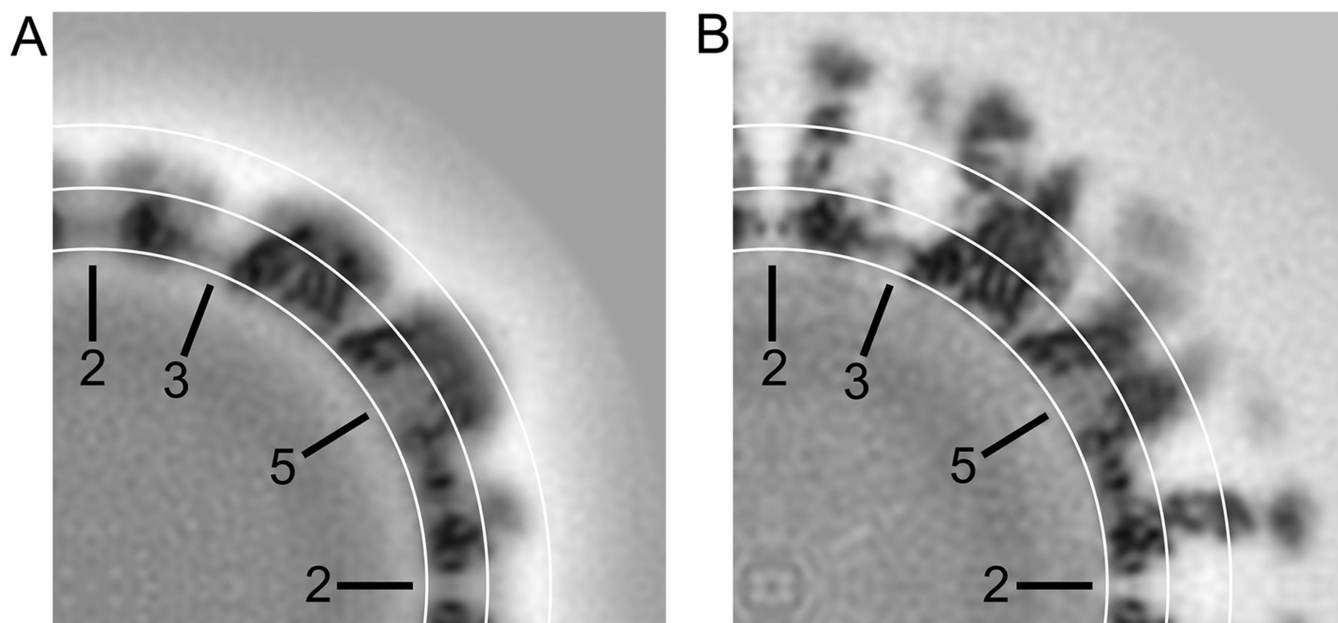


FIG 4 Central sections show Fab-induced conformational changes to HPV. The three white circles indicate radii of 220, 260, and 300 Å on the central sections of the 3D maps of the altered capsid (A) and corresponding capsid-Fab complex (B). Significant differences were visualized within the 260- to 300-Å radii. Specifically, the HPV16 capsid had smeared density, whereas within the same radii of the complex map there were sharp, distinct features, indicating that surface loop structures had become more ordered upon Fab binding. Icosahedral symmetry axes are indicated in the central section, and the symmetry bars represent 50 nm.

used as a reference, against which 10% of the altered particles were selected for an experimental reconstruction. However, the experiment failed to identify a subset of particles because the resulting map was identical, albeit with lower resolution (15 Å), to the reconstruction that used 70% of the altered particles (Fig. 3C). A visual inspection agreed with the quantification (correlation coefficient, 0.99) showing that both maps (reconstructed from 10% and 70%) had surface structural characteristics similar to those of an immature capsid. Therefore, the altered HPV16 structure is not an average of mixed populations of mature and altered particles but an averaged representation of a homogeneous set of altered particles with a common diameter but with altered or flexible surface loops.

Fab binding induced conformational changes to the altered capsid. Fitting of the HPV pentamer and H16.V5 Fab variable-domain structures into the altered-capsid-Fab complex proceeded using the approach described for the mature-virus-Fab structure and achieved the same result (data not shown). However, there were significant structural differences observed in the altered capsid. A central section of the altered capsid revealed low-contrast densities for the distal portion of the capsomers (radii, 260 to 300 Å) and a high contrast for the region of the capsomers adjacent to the capsid floor (radii, 220 to 260 Å) (Fig. 4A), whereas the mature virus map had more consistent contrast (data not shown). The low- and high-contrast densities of the altered capsid indicated disordered surface loop structures and ordered β -strand structures, respectively. After the Fab binding, the electron densities of the distal portion became as highly organized as the capsid floor region, so that the electron densities corresponding to the whole capsomer became distinguishable (Fig. 4B).

H16.V5 Fab binding induced conformational changes to the surface loops. To dissect the Fab-induced conformation change

on the altered capsid, radial projections of the four reconstructions were analyzed (Fig. 5). The 3D map of the altered capsid projected low-contrast capsomeric structures at a radius of 280 Å that were smeared and featureless, resulting in the loss of the usual pointed star-shaped morphology (Fig. 5A). In contrast, the projection of the altered-capsid-Fab complex at the same radius showed high-contrast, sharp density and a pronounced star-shaped morphology (Fig. 5B). Furthermore, after the binding of Fab, the depressions at the centers of the capsomers were significantly enhanced, with a distinct separation of the surface loops (Fig. 5B). However, in the altered-capsid-Fab complex, the pentavalent capsomers did not display the same clear high-contrast features as the hexavalent capsomers (Fig. 5B). This low contrast of the pentavalent capsomers may indicate that the altered surface loop structure is not a temporary phenomenon at the high concentration, which might be recovered upon dilution of the sample, but an enduring structural change of the surface loops. The distinct conformational changes initiated by Fab binding that were obvious in the altered form were not clearly seen in the mature virus and its corresponding Fab complex (Fig. 5C and D). This lesser structural change may be due to the virus having somewhat more structured loops prior to Fab association; thus, the binding of the Fab induced little change. Another possibility is that the hyperstabilization of the loops was not visualized in the mature-virus structure due to the lower quality of the map compared to the altered-capsid map (see Materials and Methods).

H16.V5 Fab binding stabilized the structure of the invading-arm and intercapsomeric connections. The L1 C-terminal invading arm extends from the originating capsomer at a radius of 257 Å, where it crosses the capsid floor to connect with the neighboring capsomer. From the attachment site, the most distal portion of the C terminus stretches back above the

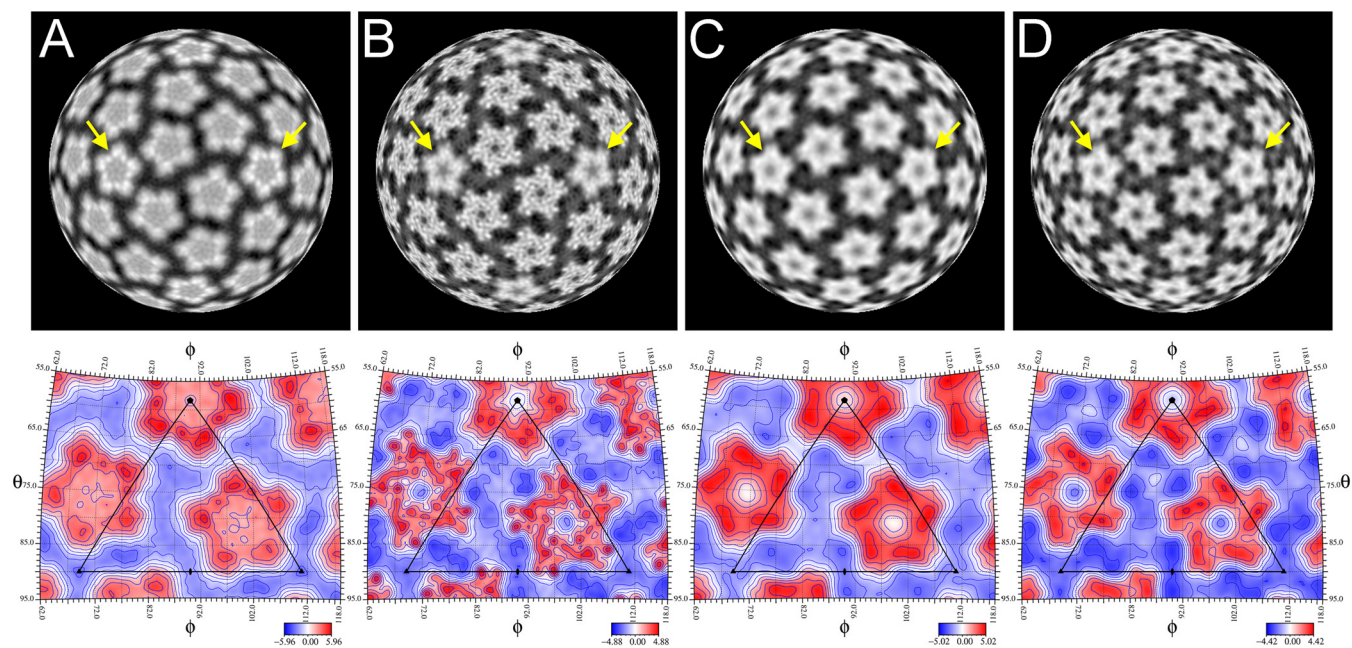


FIG 5 The conformational change induced by Fab binding is illustrated by the alteration of densities and is more significant in the altered capsid than in mature virus. For the top panels, the reconstructions of the altered capsid (A), the capsid-Fab complex (B), the mature virus (C), and the virus-Fab complex (D) were radially projected at 280 Å. The pentavalent capsomers are indicated by yellow arrows. In altered capsids, Fab binding induced conformational changes on the hexavalent capsomers, whereas the change was attenuated on the pentavalent capsomers (A and B). The Fab-induced conformational changes were more significant in the altered capsid than in the mature virus (C and D). The bottom panels represent stereographic projections at the same radii on which the polar angles θ and ϕ represent latitude and longitude, respectively. The icosahedral asymmetric unit of the virus is indicated by the black triangular boundary, and the projections are colored according to the electron density height in the corresponding color keys.

capsid floor at a radius of 264 Å to rejoin the originating capsomer, forming a structure called the “suspended bridge” (18). Radial projections of the cryo-EM maps at radii of 257 and 264 Å show these invading-arm densities (Fig. 6, middle and top)

(18, 24), which were more ordered in the altered-capsid-Fab complex reconstruction than in the altered capsid alone (Fig. 6A and B). This ordered density suggests that Fab binding stabilized the C-terminal arms. The same significant density differ-

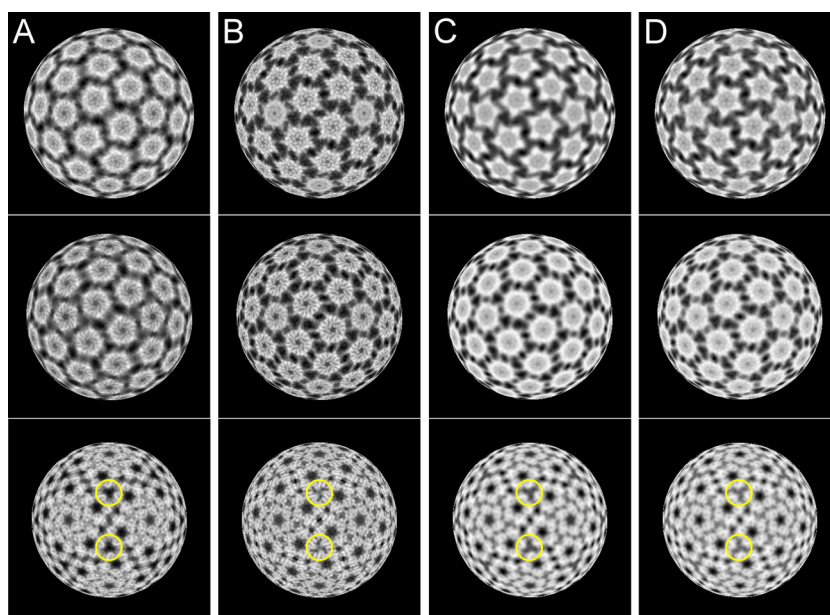


FIG 6 Fab-induced stabilization of the capsid was shown by enhanced intercapsomeric connections. The reconstructions of the altered capsid (A), the capsid-Fab complex (B), the mature virus (C), and the virus-Fab complex (D) were radially projected at 265 Å (top), 257 Å (middle), and 240 Å (bottom) to show the invading arms and the capsid floor regions of the capsids. The invading-arm structures were significantly enhanced, and the electron densities at the icosahedral 3-fold axes of the capsid floor (yellow circles) were rearranged after Fab binding in altered capsids. The standard orientations of the capsids are the same as in Fig. 5.

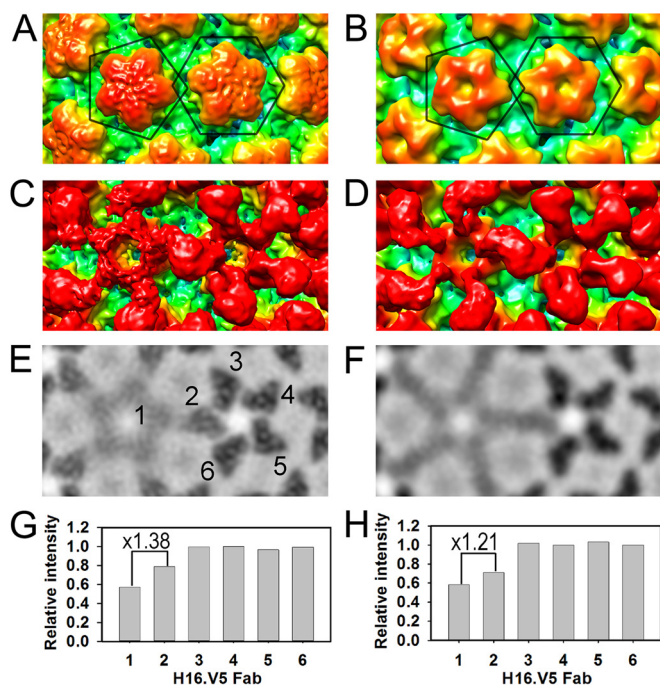


FIG 7 Fab preference for hexavalent capsomers was more pronounced in the altered HPV capsids. The pentavalent and hexavalent capsomers (outlined in black) of the 3D reconstructions of altered (A) and mature (B) virus showed marked density differences. (C and D) The capsid-Fab complexes had different Fab densities on the pentavalent and hexavalent capsomers, a difference that was more pronounced for the altered-capsid-Fab complex. The rendered surfaces were radially colored according to the color key in Fig. 1. (E and F) Radial projections of the capsid-Fab complex maps at the 310-Å radii show that Fabs bound on pentavalent capsomers have weaker intensities than those bound on hexavalent capsomers. (G and H) The relative mean intensities of the six Fabs bound on an icosahedral asymmetric unit of the capsid were measured and normalized by the mean intensity of Fab-4 (numbers are shown in panel E). The relative intensities of the Fab-1 and -2 quantify the preference of Fab for the binding sites on altered capsid (G) and mature virus (H).

ence was not observed in the mature-virus and virus-Fab complex maps (Fig. 6C and D).

Between unbound and Fab-bound capsids, the most significant difference between structures on the capsid floor was found at the icosahedral 3-fold axis, where three L1 N-terminal arms contact each other (24). Projections at a radius of 240 Å (Fig. 6, bottom) showed that there was a notable lack of capsid floor density for altered capsid (Fig. 6A), whereas the same region of the altered-capsid-Fab complex was filled with well-defined densities (Fig. 6B), suggesting stabilization of the N-terminal arms. Thus, the Fab-induced conformational changes were propagated from the surface loops down to the capsid floor. For the mature virus and its virus-Fab complex, the changes to capsid floor density were less significant (Fig. 6C and D).

The virus-Fab complex maps showed different occupancy of Fab bound to the pentavalent capsomers. The puffy capsomer of the altered capsid was significantly different from the star-shaped capsomer of the mature virus (Fig. 7A and B). Despite the resolution differences, the overall features between the complex maps (Fig. 1B and 3D) were similar except for the Fab densities on the pentavalent capsomers (Fig. 7C and D). On the mature virus, these Fab densities were stronger and maintained an unbroken

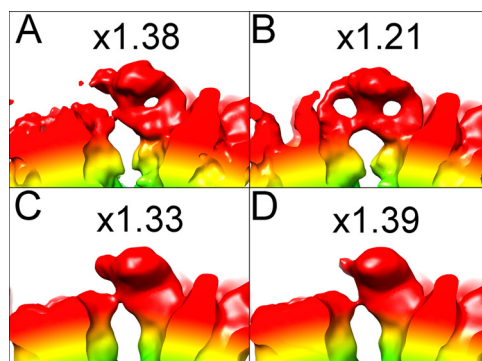


FIG 8 Longer Fab incubation with virus enhanced the Fab binding to the hexavalent capsomer. Cryo-EM densities for the Fab-1 (left) and Fab-2 (right) on the pentavalent and hexavalent capsomers are shown for altered-virus-Fab (A) and mature-virus-Fab (B to D) complexes. The mature virus was incubated for 5 min (B), 1 h (C), and 72 h (D). The relative intensities of Fab-1 and -2 (numbers in each panel) indicate that as the incubation time increased, the Fab binding to the hexavalent capsomers increased. The rendered surfaces were radially colored according to the color key in Fig. 1 and presented at a contour level of 1.0 σ above background.

shape, whereas in comparison, the altered capsids had weaker pentavalent Fab densities and were more irregular in shape. For both capsids, this partial occupancy was due to steric collision between Fab-1 and -2 (Fig. 2) and was illustrated in the radial projection at 310 Å, which showed that the competing Fabs had weaker intensities than the other four noncompeting Fabs (Fig. 7E and F). To quantify the difference, Fab densities were segmented, and the mean intensities of each Fab on pentavalent and hexavalent capsomers were compared (Fig. 7G and H). In both reconstructions, Fab-3 to Fab-6 showed consistent intensities, whereas Fab-1 showed the lowest intensity in both maps. However, the difference in intensity between Fab-1 and Fab-2 was greater in the altered-capsid-Fab complex (Fig. 7G) than in the mature complex (Fig. 7H) (ratios of Fab-2 to Fab-1, 1.38 versus 1.21), indicating a further-reduced occupancy of the Fab-1 in the altered HPV16-Fab structure.

Longer incubation times for Fab illustrated hyperstabilization of the capsomer. Our mature-virus-Fab map differed from the complex map in a previous study in which the H16.V5 Fabs bound exclusively to hexavalent capsomers (17). If the Fab mechanism of neutralization induces hyperstabilization, longer incubation times may affect the binding preference for the sites on pentavalent and hexavalent capsomers. For our reconstruction, the capsids and Fabs were incubated for 5 min (see Materials and Methods) (Fig. 6B). Therefore, we tested longer incubation times (1 h and 72 h) to assess changes in Fab binding between the pentavalent and hexavalent capsomers. The 3D reconstructions corresponding to the two time points revealed that as the incubation time increases, the Fab densities on the pentavalent capsomers diminish (Fig. 8C and D).

DISCUSSION

The conformational epitope of H16.V5 includes multiple loops. The pseudoatomic model for the virus-Fab complex allowed precise interpretation of the H16.V5 epitope (Fig. 2). The footprint is consistent with previous studies that showed FG (266 to 297) and HI (339 to 365) loops are critical for the H16.V5 binding (30). In addition, we identified two previously unreported loops, BC and

DE, on the viral surface that contribute to the epitope (Fig. 2D). In total, the footprint includes five intertwined loops that are situated side by side (13). By binding these five loops simultaneously, the Fab may reinforce the association between the two L1 proteins.

The mature- and altered-capsid reconstructions were generated from homogeneous particles. Unlike what was seen for L1-only VLPs, our preparations of quasivirus resulted in homogeneous capsids, perhaps due to the rigorous purification method. The altered capsid we inadvertently captured has a structure different from that of the mature virus (18, 25) and shares some features of the immature VLP characterized previously (25). The high quality of the altered-capsid map and our inability to select a subset of particles suggests that the data were uniformly “altered.” Likely the formation of the altered state was triggered by the high particle concentration, as this treatment marked the only difference in handling of this preparation and all previous or subsequent ones. Although we have not characterized the exact mechanism of the alteration of the HPV16 capsid, our finding shows that the highly concentrated virus underwent a conformational change, resulting in flexible loops consistent with the immature form of VLP.

Binding of H16.V5 Fab converted the HPV16 altered capsid. The Fab binding to the altered capsid induced conformational changes that converted the whole capsid structure into a more ordered conformation. Specifically, the Fab-induced conformational change was propagated from the surface loops (Fig. 5) to the capsid floor, as shown by the more ordered intercapsomeric interactions, including the distal invading-arm structures (Fig. 6). Prior to Fab binding, the C-terminal arms were less ordered, as indicated by the weak density; however, it is unlikely that the disulfide bond between C175 and C426 was disrupted, because reducing conditions were not present. The enhanced rigidity of the C-terminal arm structures in the virus-Fab complex probably indicates a restoration of the capsomeric structure to a more ordered form.

Fab binding induced different degrees of conformational change. For both the altered and mature complex maps, hexavalent and pentavalent capsomers had different numbers of Fabs bound (Fig. 3G and H). In the altered-capsid–Fab complex map, the Fab-induced conformational changes found at the apical surfaces of the pentavalent capsomers were not as distinct as those in the hexavalent capsomers (Fig. 5), even though the Fabs bound to the pentavalent capsomers, albeit with lower occupancy (Fig. 7). Thus, the degree of organization of individual capsomers induced by Fab binding correlated directly with the number of Fab molecules bound. The conformational changes of the surface loops correlated with the higher occupancy of the Fabs; thus, the effects manifested fully only on the hexavalent capsomers and were not conferred to pentavalent capsomers (Fig. 4B). This hexavalent-limited structural alteration indicates that the conformational changes are induced by the binding of multiple Fabs.

Fab detects a difference between pentavalent and hexavalent capsomers. In both altered and mature-virus–Fab complexes, there was preferential binding of Fab-2 (binding site 2 on the hexavalent capsomer) over Fab-1 (binding site 1 on the pentavalent capsomers) (Fig. 7). This preferred binding of Fab-2 implies that the affinity is different between the two binding sites. A difference in affinity might exist intrinsically or be induced by Fab binding. Because of obvious differences between the 3D structures (Fig. 7A and B) (25), the altered and mature capsids likely have different antigenicity. An interpretation using the high-resolution

map of BPV did not reveal any structural differences between the two Fab binding sites (24), and no significant difference was defined between capsomers of our altered and mature capsids. However, we cannot rule out the possibility that the hexavalent and pentavalent capsomers have intrinsic differences (51), especially in the altered capsid. Such inherent differences might be due to quasiequivalent environments and subtle enough to be below the level of detection at the current resolutions.

Alternatively, preferred hexavalent binding of Fab might be caused by a complementarity mechanism whereby the initial Fab binding events (Fab-3 to -6) led to the stabilization of binding site 2 in a ripple effect, which induced hyperstabilization. Both of these intrinsic and extrinsic mechanisms explain preferential binding of the Fab, and a combination of the two mechanisms is also possible. In contrast to our result, a previous cryo-EM reconstruction of HPV16 VLP–Fab complex showed that H16.V5 Fab bound to the hexavalent capsomers exclusively (17). This finding may have been due to the low resolution of the map and the partial occupancy of Fab and different experimental conditions, such as incubation time and temperature. Our reconstruction resulted in a similar appearance after a low-pass filter was applied (data not shown). Alternatively, the presence of L2 in our QV capsid might contribute to alterations in the loops between the pentavalent and hexavalent capsomers compared to the L1-only VLP.

Fab binding changes over time because binding induces a conformational change in the surface loops. Our 3D reconstructions of the virus–Fab complex at different time points revealed that as the incubation time increases, the occupation of Fab on the hexavalent capsomer is enhanced, while binding to the pentavalent capsomer decreases (Fig. 8). This preference for the hexavalent over the pentavalent site supports a hyperstabilization model: longer incubation of the mature virion with Fabs reflects the potential changes of the binding equilibrium between the two binding sites and would result in more preferential binding to the hexavalent capsomer. Our structural analysis also demonstrates that Fab can distinguish the small differences on the binding sites that cannot be detected in the structure alone.

ACKNOWLEDGMENTS

This project was funded, in part, by The Gittlen Memorial Golf Tournament and by a grant with the Pennsylvania Department of Health using Tobacco CURE Funds and an NIH SIG 1S10RR031780-01A1.

We thank the Microscopy Imaging Shared Core Facility at the Pennsylvania State University College of Medicine.

H.L., N.D.C., and S.H. designed the research; S.A.B. and S.M.B. produced virus and antibodies; J.D.Y., R.E.A., A.M.M., and J.F.C. collected EM data; H.L. processed and analyzed data; J.G. helped with scientific discussion; H.L. and S.H. wrote the paper.

REFERENCES

- Walboomers JM, Jacobs MV, Manos MM, Bosch FX, Kummer JA, Shah KV, Snijders PJ, Peto J, Meijer CJ, Muñoz N. 1999. Human papillomavirus is a necessary cause of invasive cervical cancer worldwide. *J Pathol* 189:12–19. [http://dx.doi.org/10.1002/\(SICI\)1096-9896\(199909\)189:1<12::AID-PATH431>3.0.CO;2-F](http://dx.doi.org/10.1002/(SICI)1096-9896(199909)189:1<12::AID-PATH431>3.0.CO;2-F).
- Woodman CBJ, Collins SI, Young LS. 2007. The natural history of cervical HPV infection: unresolved issues. *Nat Rev Cancer* 7:11–22. <http://dx.doi.org/10.1038/nrc2050>.
- zur Hausen H. 2009. Papillomaviruses in the causation of human cancers—a brief historical account. *Virology* 384:260–265. <http://dx.doi.org/10.1016/j.virol.2008.11.046>.
- Lorincz AT, Reid R, Jenson AB, Greenberg MD, Lancaster W, Kurman RJ. 1992. Human papillomavirus infection of the cervix: relative risk as-

- sociations of 15 common anogenital types. *Obstet Gynecol* 79:328–337. <http://dx.doi.org/10.1097/00006250-199203000-00002>.
5. Bosch FX, Manos MM, Muñoz N, Sherman M, Jansen AM, Peto J, Schiffman MH, Moreno V, Kurman R, Shan KV. 1995. Prevalence of human papillomavirus in cervical cancer: a worldwide perspective. *J Natl Cancer Inst* 87:796–802. <http://dx.doi.org/10.1093/jnci/87.11.796>.
6. Koutsky LA, Ault KA, Wheeler CM, Brown DR, Barr E, Alvarez FB, Chiacchierini LM, Jansen KU. 2002. A controlled trial of a human papillomavirus type 16 vaccine. *N Engl J Med* 347:1645–1651. <http://dx.doi.org/10.1056/NEJMoa020586>.
7. Lowy DR, Solomon D, Hildesheim A, Schiller JT, Schiffman M. 2008. Human papillomavirus infection and the primary and secondary prevention of cervical cancer. *Cancer* 113:1980–1993. <http://dx.doi.org/10.1002/cncr.23704>.
8. Hagensee ME, Yaegashi N, Galloway DA. 1993. Self-assembly of human papillomavirus type 1 capsids by expression of the L1 protein alone or by coexpression of the L1 and L2 capsid proteins. *J Virol* 67:315–322.
9. Buck CB, Pastrana DV, Lowy DR, Schiller JT. 2004. Efficient intracellular assembly of papillomaviral vectors. *J Virol* 78:751–757. <http://dx.doi.org/10.1128/JVI.78.2.751-757.2004>.
10. Culp TD, Cladel NM, Balogh KK, Budgeon LR, Mejia AF, Christensen ND. 2006. Papillomavirus particles assembled in 293TT cells are infectious in vivo. *J Virol* 80:11381–11384. <http://dx.doi.org/10.1128/JVI.01328-06>.
11. Buck CB, Cheng N, Thompson CD, Lowy DR, Steven AC, Schiller JT, Trus BL. 2008. Arrangement of L2 within the papillomavirus capsid. *J Virol* 82:5190–5197. <http://dx.doi.org/10.1128/JVI.02726-07>.
12. Bishop B, Dasgupta J, Klein M, Garcea RL, Christensen ND, Zhao R, Chen XS. 2007. Crystal structures of four types of human papillomavirus L1 capsid proteins: understanding the specificity of neutralizing monoclonal antibodies. *J Biol Chem* 282:31803–31811. <http://dx.doi.org/10.1074/jbc.M706380200>.
13. Chen XS, Garcea RL, Goldberg I, Casini G, Harrison SC. 2000. Structure of small virus-like particles assembled from the L1 protein of human papillomavirus 16. *Mol Cell* 5:557–567. [http://dx.doi.org/10.1016/S1097-2765\(00\)80449-9](http://dx.doi.org/10.1016/S1097-2765(00)80449-9).
14. Dasgupta J, Bienkowska-Haba M, Ortega ME, Patel HD, Bodevin S, Spillmann D, Bishop B, Sapp M, Chen XS. 2011. Structural basis of oligosaccharide receptor recognition by human papillomavirus. *J Biol Chem* 286:2617–2624. <http://dx.doi.org/10.1074/jbc.M110.160184>.
15. Baker TS, Newcomb WW, Olson NH, Cowser LM, Olson C, Brown JC. 1991. Structures of bovine and human papillomaviruses. Analysis by cryo-electron microscopy and three-dimensional image reconstruction. *Bio-phys J* 60:1445.
16. Hagensee ME, Olson NH, Baker TS, Galloway DA. 1994. Three-dimensional structure of vaccinia virus-produced human papillomavirus type 1 capsids. *J Virol* 68:4503–4505.
17. Zhao Q, Potter CS, Carragher B, Lander G, Sworen J, Towne V, Abraham D, Duncan P, Washabaugh MW, Sitrin RD. 2014. Characterization of virus-like particles in GARDASIL® by cryo transmission electron microscopy. *Hum Vaccin Immunother* 10:734–739. <http://dx.doi.org/10.4161/hv.27316>.
18. Cardone G, Moyer AL, Cheng N, Thompson CD, Dvoretzky I, Lowy DR, Schiller JT, Steven AC, Buck CB, Trus BL. 2014. Maturation of the human papillomavirus 16 capsid. *mBio* 5:e01104–14. <http://dx.doi.org/10.1128/mBio.01104-14>.
19. Carter JJ, Wipf GC, Benki SF, Christensen ND, Galloway DA. 2003. Identification of a human papillomavirus type 16-specific epitope on the C-terminal arm of the major capsid protein L1. *J Virol* 77:11625–11632. <http://dx.doi.org/10.1128/JVI.77.21.11625-11632.2003>.
20. Ludmerer SW, Benincasa D, Mark GE. 1996. Two amino acid residues confer type specificity to a neutralizing, conformationally dependent epitope on human papillomavirus type 11. *J Virol* 70:4791–4794.
21. Ludmerer SW, Benincasa D, Mark GE, Christensen ND. 1997. A neutralizing epitope of human papillomavirus type 11 is principally described by a continuous set of residues which overlap a distinct linear, surface-exposed epitope. *J Virol* 71:3834–3839.
22. Roth SD, Sapp M, Streeck RE, Selinka H-C. 2006. Characterization of neutralizing epitopes within the major capsid protein of human papillomavirus type 33. *J Virol* 80:383. <http://dx.doi.org/10.1186/1743-422X-3-83>.
23. White WI, Wilson SD, Palmer-Hill FJ, Woods RM, Ghim S, Hewitt LA, Goldman DM, Burke SJ, Jensen AB, Koenig S. 1999. Characterization of a major neutralizing epitope on human papillomavirus type 16 L1. *J Virol* 73:4882–4889.
24. Wolf M, Garcea RL, Grigorieff N, Harrison SC. 2010. Subunit interactions in bovine papillomavirus. *Proc Natl Acad Sci U S A* 107:6298–6303. <http://dx.doi.org/10.1073/pnas.0914604107>.
25. Buck CB, Trus BL. 2012. The papillomavirus virion: a machine built to hide molecular Achilles' heels, p 403–422. *In* Rossmann MG, Rao VB (ed), *Viral molecular machines*. Springer, Boston, MA.
26. Buck CB, Thompson CD, Pang YYS, Lowy DR, Schiller JT. 2005. Maturation of papillomavirus capsids. *J Virol* 79:2839–2846. <http://dx.doi.org/10.1128/JVI.79.5.2839-2846.2005>.
27. Conway MJ, Alam S, Ryndock EJ, Cruz L, Christensen ND, Roden RBS, Meyers C. 2009. Tissue-spanning redox gradient-dependent assembly of native human papillomavirus type 16 virions. *J Virol* 83:10515–10526. <http://dx.doi.org/10.1128/JVI.00731-09>.
28. Li M, Beard P, Estes PA, Lyon MK, Garcea RL. 1998. Intercapsomeric disulfide bonds in papillomavirus assembly and disassembly. *J Virol* 72:2160–2167.
29. Christensen ND, Dillner J, Eklund C, Carter JJ, Wipf GC, Reed CA, Cladel NM, Galloway DA. 1996. Surface conformational and linear epitopes on HPV-16 and HPV-18 L1 virus-like particles as defined by monoclonal antibodies. *Virology* 223:174–184. <http://dx.doi.org/10.1006/viro.1996.0466>.
30. Christensen ND, Cladel NM, Reed CA, Budgeon LR, Embers ME, Skulsky DM, McClements WL, Ludmerer SW, Jansen KU. 2001. Hybrid papillomavirus L1 molecules assemble into virus-like particles that reconstitute conformational epitopes and induce neutralizing antibodies to distinct HPV types. *Virology* 291:324–334. <http://dx.doi.org/10.1006/viro.2001.1220>.
31. Wang X, Wang Z, Christensen ND, Dillner J. 2003. Mapping of human serum-reactive epitopes in virus-like particles of human papillomavirus types 16 and 11. *Virology* 311:213–221. [http://dx.doi.org/10.1016/S0042-6822\(03\)00179-X](http://dx.doi.org/10.1016/S0042-6822(03)00179-X).
32. Shank-Retzlaff M, Wang F, Morley T, Anderson C, Hamm M, Brown M, Rowland K, Pancari G, Zorman J, Lowe R. 2005. Correlation between mouse potency and in vitro relative potency for human papillomavirus type 16 virus-like particles and Gardasil® vaccine samples. *Hum Vaccin* 1:191–197. <http://dx.doi.org/10.4161/hv.1.5.2126>.
33. Day PM, Thompson CD, Buck CB, Pang Y-YS, Lowy DR, Schiller JT. 2007. Neutralization of human papillomavirus with monoclonal antibodies reveals different mechanisms of inhibition. *J Virol* 81:8784–8792. <http://dx.doi.org/10.1128/JVI.00552-07>.
34. Brendle SA, Culp TD, Broutian TR, Christensen ND. 2010. Binding and neutralization characteristics of a panel of monoclonal antibodies to human papillomavirus 58. *J Gen Virol* 91:1834–1839. <http://dx.doi.org/10.1099/vir.0.017228-0>.
35. Mejia AF, Culp TD, Cladel NM, Balogh KK, Budgeon LR, Buck CB, Christensen ND. 2006. Preclinical model to test human papillomavirus virus (HPV) capsid vaccines in vivo using infectious HPV/cotton tail rabbit papillomavirus chimeric papillomavirus particles. *J Virol* 80:12393–12397. <http://dx.doi.org/10.1128/JVI.01583-06>.
36. Christensen ND, Kreider JW. 1990. Antibody-mediated neutralization in vivo of infectious papillomaviruses. *J Virol* 64:3151–3156.
37. Christensen ND, Kirnbauer R, Schiller JT, Ghim SJ, Schlegel R, Jensen AB, Kreider JW. 1994. Human papillomavirus types 6 and 11 have antigenically distinct strongly immunogenic conformationally dependent neutralizing epitopes. *Virology* 205:329–335. <http://dx.doi.org/10.1006/viro.1994.1649>.
38. Wang Z, Raifu M, Howard M, Smith L, Hansen D, Goldsby R, Ratner D. 2000. Universal PCR amplification of mouse immunoglobulin gene variable regions: the design of degenerate primers and an assessment of the effect of DNA polymerase 3' to 5' exonuclease activity. *J Immunol Methods* 233:167–177. [http://dx.doi.org/10.1016/S0022-1759\(99\)00184-2](http://dx.doi.org/10.1016/S0022-1759(99)00184-2).
39. Tivol WF, Briegel A, Jensen GJ. 2008. An improved cryogen for plunge freezing. *Microsc Microanal* 14:375–379. <http://dx.doi.org/10.1017/S1431927608080781>.
40. Yan X, Sinkovits RS, Baker TS. 2007. AUTO3DEM—an automated and high throughput program for image reconstruction of icosahedral particles. *J Struct Biol* 157:73–82. <http://dx.doi.org/10.1016/j.jsb.2006.08.007>.
41. Tang G, Peng L, Baldwin PR, Mann DS, Jiang W, Rees I, Ludtke SJ. 2007. EMAN2: an extensible image processing suite for electron microscopy. *J Struct Biol* 157:38–46. <http://dx.doi.org/10.1016/j.jsb.2006.05.009>.
42. Yan X, Dryden KA, Tang J, Baker TS. 2007. Ab initio random model method facilitates 3D reconstruction of icosahedral particles. *J Struct Biol* 157:211–225. <http://dx.doi.org/10.1016/j.jsb.2006.07.013>.

43. Pettersen EF, Goddard TD, Huang CC, Couch GS, Greenblatt DM, Meng EC, Ferrin TE. 2004. UCSF Chimera—a visualization system for exploratory research and analysis. *J Comput Chem* 25:1605–1612. <http://dx.doi.org/10.1002/jcc.20084>.
44. Whitelegg NR, Rees AR. 2000. WAM: an improved algorithm for modelling antibodies on the WEB. *Protein Eng* 13:819–824. <http://dx.doi.org/10.1093/protein/13.12.819>.
45. Wriggers W. 2010. Using Situs for the integration of multi-resolution structures. *Biophys Rev* 2:21–27. <http://dx.doi.org/10.1007/s12551-009-0026-3>.
46. Saff EB, Kuijlaars AB. 1997. Distributing many points on a sphere. *Math Intell* 19:5–11.
47. Xiao C, Rossmann MG. 2007. Interpretation of electron density with stereographic roadmap projections. *J Struct Biol* 158:182–187. <http://dx.doi.org/10.1016/j.jsb.2006.10.013>.
48. Pintilie GD, Zhang J, Goddard TD, Chiu W, Gossard DC. 2010. Quantitative analysis of cryo-EM density map segmentation by watershed and scale-space filtering, and fitting of structures by alignment to regions. *J Struct Biol* 170:427–438. <http://dx.doi.org/10.1016/j.jsb.2010.03.007>.
49. Belnap DM, Olson NH, Cladel NM, Newcomb WW, Brown JC, Kreider JW, Christensen ND, Baker TS. 1996. Conserved features in papillomavirus and polyomavirus capsids. *J Mol Biol* 259:249–263. <http://dx.doi.org/10.1006/jmbi.1996.0317>.
50. Hafenstein S, Bowman VD, Sun T, Nelson CDS, Palermo LM, Chipman PR, Battisti AJ, Parrish CR, Rossmann MG. 2009. Structural comparison of different antibodies interacting with parvovirus capsids. *J Virol* 83: 5556–5566. <http://dx.doi.org/10.1128/JVI.02532-08>.
51. Booy FP, Roden R, Greenstone HL, Schiller JT, Trus BL. 1998. Two antibodies that neutralize papillomavirus by different mechanisms show distinct binding patterns at 13 Å resolution. *J Mol Biol* 281:95–106. <http://dx.doi.org/10.1006/jmbi.1998.1920>.